Additional Information

Exploring the high-pressure behavior of the three known polymorphs of BiPO$_4$: Discovery of a new polymorph

D. Errandonea[1,*], O. Gomis[2], D. Santamaría-Perez[1,3], B. García-Domene[1], A. Muñoz[4], P. Rodríguez-Hernández[4], S.N. Achary[5], A.K. Tyagi[5], and C. Popescu[6]

[1]*Departamento de Física Aplicada-ICMUV, MALTA Consolider Team, Universidad de Valencia, Edificio de Investigación, C/Dr. Moliner 50, Burjassot, 46100 Valencia, Spain*

[2]C*entro de Tecnologías Físicas, MALTA Consolider Team, Universitat Politècnica de Valencia, 46022 Valencia, Spain*

[3]*Earth Sciences Department, Univ. College London, UK*

[4]*Departamento de Física, Instituto de Materiales y Nanotecnología, MALTA Consolider Team, Universidad de La Laguna, La Laguna 38205, Tenerife, Spain*

[5]*Chemistry Division, Bhabha Atomic Research Centre, Trombay, Mumbai 400085, India*

[6]*CELLS-ALBA Synchrotron Light Facility, Cerdanyola, 08290 Barcelona, Spain*

Abstract

We have studied the structural behavior of bismuth phosphate under compression. We performed x-ray powder diffraction measurements up to 31.5 GPa and *ab initio* calculations. Experiments were carried out on different polymorphs: trigonal (phase I) and monoclinic (phases II and III). Phases I and III, at low pressure (P < 0.2 − 0.8 GPa), transform into phase II, which has a monazite-type structure. At room temperature, this polymorph is stable up to 31.5 GPa. Calculations support these findings and predict the occurrence of an additional transition from the monoclinic monazite-type to a tetragonal scheelite-type structure (phase IV). This transition was experimentally found after the simultaneous application of pressure (28 GPa) and temperature (1500 K), suggesting that at room temperature the transition might by hindered by kinetic barriers. Calculations also predict an additional phase transition at 52 GPa, which exceeds the

* Corresponding author, email: daniel.errandonea@uv.es

28 maximum pressure achieved in the experiments. This transition is from phase IV to an

29 orthorhombic barite-type structure (phase V). We also studied the axial and bulk

30 compressibility of $BiPO_4$. Room-temperature pressure-volume equations of state are

31 reported. $BiPO_4$ was found to be more compressible than isomorphic rare-earth

32 phosphates. The discovered phase IV was determined to be the less compressible

33 polymorph of $BiPO_4$. On the other hand, the theoretically predicted phase V has a bulk

34 modulus comparable with that of monazite-type $BiPO_4$. Finally, the isothermal

35 compressibility tensor for the monazite-type structure is reported at 2.4 GPa showing

36 that the direction of maximum compressibility is in the (0 1 0) plane at approximately

37 15º (21º) to the *a* axis for the case of our experimental (theoretical) study.

38

2

I.   Introduction

Bismuth phosphate ($BiPO_4$) is a multifunctional material with diverse applications. It is used as catalyst and photocatalyst, ion and humidity sensor, microwave dielectric, host for luminescent ions, and in the separation and immobilization of radioactive elements [1 − 9]. In contrast with related phosphates, $BiPO_4$ exhibits a rich structural polymorphism depending on preparation method [10]. In particular, three different crystal phases are known for $BiPO_4$, a trigonal structure (phase I) and two monoclinic structures which are obtained at low- (phase II) and high-temperature (phase III). The three structures are shown in Fig. 1. Phase II is stable under ambient conditions [10]. Its crystal structure belongs to space group (SG) $P2_1/n$, has four formula units per unit cell (Z = 4), and is isomorphic to the monazite structure [11]. Phase III is synthesized at high temperature [10] but can be recovered as a metastable phase at ambient conditions. The crystal structure of phase III is isomorphic to that of $SbPO_4$ and belongs to SG $P2_1/m$ (Z = 2). Phase I is prepared by precipitation from an aqueous solution and the H_2O molecules play a crucial role in the retention of this phase at ambient conditions [10]. The crystal structure of phase I belongs to SG $P3_121$ (Z = 3). The structural relation among the three polymorphs has been discussed previously [10]. In particular, phases I and III consist of tetrahedral PO_4 groups and highly distorted eight-coordinated BiO_8 polyhedral units. In the case of phase II (monazite), the BiO_8 unit can be considered to be transformed into a BiO_9 polyhedron with eight Bi-O bonds within 2.36 to 2.70 Å and an additional long Bi-O bond at 3.02 Å.

Monazite-type oxides exist in nature. They are important accessory minerals in granitoids and rhyolites and are present in plutonic and metamorphic rocks. Therefore, the knowledge of the high-pressure (HP) structural behavior of monazite-type and related oxides is very relevant not only for technological applications, but also for

mineral physics and chemistry as well as for petrology [12]. In this regard, monazite-

type chromates [13, 14], vanadates [15, 16], and phosphates [17, 18] have been studied

under compression. However, to the best of our knowledge, $SbPO_4$-type oxides have not

been yet studied at HP. The same can be stated for phase I of $BiPO_4$. Under HP,

monazite-type chromates have been found to undergo phase transitions at 3 GPa [13,

14] while in isomorphic vanadates the transitions are detected near 10 GPa [15]. In

contrast, monazite-type phosphates are much more stable under compression. In

particular, no phase transition is detected in $GdPO_4$, $EuPO_4$, and $NdPO_4$ up to 30 GPa

and in $LaPO_4$ the onset of a structural transformation from the monazite-type to a barite-

type structure occurs at 26 GPa [17]. On top of that, monazite $CePO_4$ does not undergo

structural transitions up to 20 GPa, but its unit-cell parameters show an anomalous

pressure behavior beyond 12 GPa [18]. Therefore, it is clear that further efforts are

needed to elucidate the behavior under pressure of the different polymorphs of $BiPO_4$

and related phosphates.

Here, in order to improve the understanding of the structural properties of the

three known polymorphs of $BiPO_4$ and to explore the possible occurrence of pressure-

driven phase transitions, we have studied the HP behavior of phases I, II, and III of

$BiPO_4$ by x-ray diffraction (XRD) up to 31.5 GPa. *Ab initio* calculations were also

carried out, being obtained an excellent agreement with experiments. We have found

that phase I and phase III transform into the monazite-type structure (phase II) at low

pressure, 0.2 GPa and 0.8 GPa; respectively. Regarding phase II, calculations predict

that a phase transition to a more dense scheelite-type structure (phase IV) should occur

at 15 GPa. In contrast with this result, our room-temperature (RT) experiments found

that phase II remains stable up to 31.5 GPa. However, upon the simultaneous

application of pressure and temperature the new phase IV is obtained, suggesting that

92   kinetic barriers could hinder the II→IV phase transition. The crystal structural details of

93   the new phase have been determined. Moreover, calculations predict a phase transition

94   from phase IV to an orthorhombic phase V occurring at 52 GPa, which is a pressure 20

95   GPa higher than the maximum experimental pressure. From our studies we obtained the

96   axial and bulk compressibility for phases II and III as well as the isothermal RT P-V

97   equation of state (EOS) for phases I to V. The reported results will be discussed in

98   comparison with related phosphates.

99   **II. Experimental details**

100   Single-phase high-purity powders of $BiPO_4$ in phases I, II, and III were prepared

101   by precipitation from an aqueous solution and subsequent treatments at different

102   temperatures. Details on preparation method and sample characterization can be found

103   elsewhere [10]. With the prepared samples we carried out four RT high-pressure

104   experiments. A sample from phase III was compressed up to 28 GPa (run 1). A sample

105   from phase I was pressurized up to 21 GPa (run 2). Two samples from phase II were

106   studied up to 15.7 and 31.5 GPa (runs 3 and 4). Angle-dispersive XRD experiments

107   were carried out using a diamond-anvil cell with diamond culets of 350 μm. The

108   pressure chamber was a 100 μm hole drilled on rhenium gaskets pre-indented to 50 μm

109   thickness. The studied samples were loaded in the pressure chamber together with a few

110   W grains. The EOS of W [19] and the ruby fluorescence method [20] were used to

111   determine pressure with an accuracy of 0.1 GPa. The presence in XRD patterns of

112   Bragg peaks of W does not preclude the identification of the different crystal structure

113   of $BiPO_4$. A 16:3:1 methanol-ethanol-H_2O mixture was used a pressure transmitting

114   medium [21]. Special care was taken to occupy only a small fraction on the pressure

115   chamber with the loaded samples to reduce the possibility of sample bridging between

116   the diamond anvils [22, 23]. In situ HP XRD measurements were carried out at MSPD

117 beamline of ALBA synchrotron [24] with the exception of run 3 which was performed

118 using an Xcalibur diffractometer [25]. At ALBA the incident monochromatic beam of

119 wavelength 0.4246 Å was focused down to a 10 μm × 15 μm spot using Kirkpatrick-

120 Baez mirrors and a Rayonix CCD detector was used to collect XRD patterns. In run 3,

121 XRD patterns were obtained on a 135-mm Atlas CCD detector using $K_{\alpha 1}$:$K_{\alpha 2}$ Mo

122 radiation being the x-ray beam collimated to a diameter of 300 μm. The two

123 dimensional diffraction images collected in runs 1, 2, and 4 at ALBA were integrated

124 with the FIT2D software [26] whereas the two dimensional diffraction images collected

125 in run 3 were integrated with the CrysAllis software [27]. Structural analysis was

126 performed with PowderCell [28] and GSAS [29]. In run 1, after finalizing the

127 compression cycle at 28 GPa, a thermal annealing was carried out searching for the

128 theoretically predicted new polymorph of $BiPO_4$. For the thermal treatment we used a

129 laser-heating set-up equipped with a 100 W fiber laser (λ = 1064 nm) [30]. The sample

130 was heated to 1500 K for 2 minutes and then quenched. Temperature was calculated by

131 fitting a Planck function to the measured thermal emission spectrum of the sample [31].

132 **IIII. Theoretical methods**

133 *Ab initio* total energy simulations have been performed within the density

134 functional theory (DFT) framework as implemented in the Vienna *ab initio* simulation

135 package (VASP) [32]. VASP performs structural calculations with the plane wave

136 pseudo-potential method. In our study, the set of plane waves used was extended up to a

137 kinetic energy cutoff of 520 eV to achieve highly converged results within the

138 projector-augmented-wave scheme. In addition, the exchange-correlation energy was

139 taken in the generalized gradient approximation (GGA) with the revised Perdew–

140 Burke–Ernzerhof (PBESOL) [33] prescription which works better for $BiPO_4$ than the

141 local density approximation (LDA) [10]. Moreover, we used dense special point grids

6

142   appropriate to each structure to sample the Brillouin zone, ensuring a high convergence

143   (1–2 meV) per formula unit in the total energy of each structure as well as a precise

144   determination of the forces on the atoms. At each selected volume, the structures were

145   fully relaxed to their equilibrium configurations through the calculation of the forces on

146   the atoms and the stress tensor. In the relaxed equilibrium configuration, the forces were

147   < 0.006 eV Å^{-1}, and the deviation of the stress tensor from a diagonal hydrostatic form

148   was < 0.1 GPa. Consequently, our calculations provide a set of accurate energy,

149   volume, and pressure (E, V, P) values that can be fitted using an EOS in order to obtain

150   the equilibrium volume (V_0), bulk modulus (B_0), and its pressure derivatives (B_0' and

151   B_0''). From the calculated data it is also possible to determine the thermodynamically

152   most stable structure at different pressures [34]. With this aim, in addition to the three

153   known polymorphs of BiPO$_4$ [10], we have also included in the simulations the

154   scheelite-type (SG $I4_1/a$ Z = 4) and the barite-type (SG $Pnma$, Z = 4) structures, which

155   were previously observed as HP phases in related oxides [17, 35].

156   **IV. Results and discussion**

157   **A. High-pressure x-ray diffraction**

158   Fig. 2 shows XRD patterns measured in run 1 starting from phase III up to 22

159   GPa. In this figure, a Bragg peak associated to W can be easily identified since it has a

160   different pressure evolution than those of the sample. In this run, we found that the

161   patterns obtained from ambient pressure up to 0.6 GPa can be unequivocally assigned to

162   the SbPO$_4$-type structure. This is illustrated in Fig. 2 by the XRD patterns measured at

163   0.1 and 0.6 GPa. For the first one the residuals of the structural refinement are shown.

164   The R-factors of the refinement are $R_p = 3.01\%$ and $R_{wp} = 6.05\%$. The unit-cell

165   parameters determined at 0.1 GPa are $a = 4.871(5)$ Å, $b = 7.081(7)$ Å, $c = 4.696(5)$ Å,

166   and $\beta = 96.17(9)$º. When pressure reaches 0.8 GPa new Bragg peaks emerge which are

identified by asterisks in Fig. 2. Upon compression, these and other extra peaks gradually grow in intensity and simultaneously the peaks assigned to phase III gradually vanish. These changes can be ascribed to the onset of a phase transition, coexisting phase III and the HP phase from 0.8 to 3.0 GPa. The HP phase appears as a single phase at 4.2 GPa and can be assigned to the monazite-type structure (phase II). The structural assignment for the HP phase is supported by Rietveld refinements. The residuals of the refinement made for the data collected at 4.2 GPa are shown in Fig. 2. The R-factors of the refinement are $R_p = 3.85\%$ and $R_{wp} = 6.83\%$. The unit-cell parameters of monazite-type $BiPO_4$ at 4.2 GPa are $a = 6.646(7)$ Å, $b = 6.876(7)$ Å, $c = 6.407(5)$ Å, and $\beta = 103.3(1)°$. Pressure release from phase II at 4.2 GPa shows that the observed transition is not reversible. Upon further compression up to 28 GPa no further phase transitions are found. This can be seen in the XRD patterns measured at 22 GPa (Fig. 2) and 28 GPa (Fig. 3). As we will show in the next section, this result seems to be in conflict with our calculations, which predict that phase II should undergo a phase transition beyond 15 GPa. One possible reason for this is the presence of large kinetic barriers which hinder the occurrence of the phase transition [23]. To check this hypothesis we carried out a laser-heating annealing of our sample at 1500 K. After this treatment we found that $BiPO_4$ was crystallized in a different structure which can be assigned to the HP phase predicted by the calculations (phase IV). This is shown in Fig. 3. Rietveld refinements of the XRD pattern collected from phase IV indicated that they are consistent with a scheelite-type structure (see phase IV in Fig. 1) with $a = 4.66(1)$ Å and $c = 11.07(2)$ Å at 28 GPa, being the R-factors of the refinement $R_p = 2.74\%$ and $R_{wp} = 6.28\%$. This result agrees with the theoretically predicted structure. Upon pressure release a mixture of phase II and IV is recovered at 0.1 GPa.

191   We will summarize now the results obtained in the other experimental runs.

192   XRD patterns are not shown to avoid redundancies. In run 2 we used a sample in which

193   the trigonal phase I was observed before sample loading. Details on the characterization

194   of this sample are given in Ref. 10. However, after loading trigonal $BiPO_4$ in a DAC,

195   the monoclinic phase II was found after the first compression step at a pressure smaller

196   than 0.2 GPa. This experiment was repeated in a second DAC loaded with the same

197   sample (phase I) and the same result was obtained (phase II at 0.2 GPa). We believe that

198   this fact could be due to desorption of H_2O molecules by the effect of pressure. It is also

199   consistent with the fact that, according with calculations, phase I is thermodynamically

200   the less favored polymorph and phase II is the most stable one (see next section). Upon

201   further compression in run 2, phase II is retained up to the highest pressure covered by

202   the experiments in agreement with the results of run 1. Upon decompression phase II is

203   recovered, so the I→II transition is not reversible. Finally, runs 3 and 4 were carried out

204   directly on samples with the monazite-type structure. We found that at RT this phase II

205   is stable from ambient up to the highest pressure reached in our study, 31.5 GPa.

206   **B. *Ab initio* calculations**

207   For our theoretical study of the structural stability of $BiPO_4$ at HP, we have

208   taken into consideration previous results obtained in ABO_4 ternary oxides and the

209   packing-efficiency criterion [36]. In addition to the three known polymorphs of $BiPO_4$,

210   we have studied the relative stability of two HP candidate structures using the

211   calculation method outlined above. These two structures are isomorphic with scheelite

212   [37] and barite [38]. They are represented in Fig. 1 as phases IV and V, respectively.

213   Fig. 4 shows the total energy versus volume and enthalpy difference versus pressure

214   curves for the different structures that have been considered. The monazite-type

215   structure (phase II) is the one with the lowest energy and enthalpy at ambient pressure.

216   Therefore, monazite is the stable structure of $BiPO_4$. The calculated structural

217   parameters for $BiPO_4$ (phases I, II, and III) at ambient pressure have been reported

218   elsewhere [10] agreeing very well with the experimental results. Upon compression

219   calculations predict the occurrence of a monazite-to-scheelite phase transition at 15

220   GPa. This is a first-order transition that involves a large volume collapse ($\Delta V/V = -9$ %)

221   and according with the literature there is a large kinetic barrier associated to it [39]. This

222   could explain why in the experiments we did not found the transition at RT, but

223   detected it only after heating at 1500 K. The calculated structural parameters of phase

224   IV at 27.6 GPa are given in Table I. Additionally, in the simulations we have found that

225   at 52 GPa the barite-type structure (phase V) becomes thermodynamically more stable

226   than any other structure in $BiPO_4$. The scheelite-barite transition involves also a volume

227   collapse ($\Delta V/V = -2$ %); i.e. it is a first-order transition. The potential appearance of a

228   barite-type structure at HP in $BiPO_4$ is consistent with the results found in LaPO4 [17].

229   In our experiments, phase V has not been observed, but since the calculated transition

230   pressure is 20 GPa higher than the maximum pressure achieved in the experiments, it

231   would not be surprising that phase V could be found in future experiments beyond 50

232   GPa, in special if thermal annealing is used to overcome kinetic barriers. The calculated

233   structural details of phase V at 61 GPa are given in Table I. An interesting fact to

234   remark is that in the five polymorphs of $BiPO_4$ the P atoms are four coordinated to

235   oxygen atoms. In contrast, Bi is 8 (or 9) coordinated in the four phases found in the

236   experiments, but 12 coordinated in the barite-type structure. Thus the theoretically

237   predicted IV-V transition involves more important atomic rearrangements than I-II, III-

238   II, and II-IV transitions. In addition, the scheelite-type structure is the most symmetric

239   among the five structures studied having perfect regular PO_4 tetrahedra and a BiO_8

240   dodecahedra with only two different Bi-O distances. This structure has been found

241   before as a post-monazite structure in $TbPO_4$ and other phosphates that crystallize at

242   ambient conditions in the zircon structure [39, 40]. This consistency between different

243   studies supports the existence of the monazite-to-scheelite phase transition in $BiPO_4$.

244   **C. Room-temperature equations of state**

245   From our experiments we extracted the pressure evolution of the unit-cell

246   parameters for phases III and II of $BiPO_4$. The results are summarized in Figs. 5 and 6

247   and compared with calculations. The experimental and calculated parameters show a

248   quite good agreement. In $SbPO_4$-type $BiPO_4$ (Fig. 5), the compressibility of the three

249   axes is similar up to 3 GPa. The three axial compressibilities determined from the

250   experiments are ~ 4×10^{-3} GPa^{-1}. In addition, the β angle decreases upon compression.

251   In monazite-type $BiPO_4$ (Fig. 6) the compression is not isotropic, being a the most

252   compressible axis. As a consequence of it, a becomes very similar to c at 31.5 GPa. On

253   top of that, as in phase III, the β angle of phase II also decreases under compression.

254   The response to pressure of monazite $BiPO_4$ is similar to that found in other isomorphic

255   phosphates [17]. As in most of them, no unusual changes on the pressure dependence of

256   the unit-cell parameters have been detected in $BiPO_4$. Thus, the anomalies found in

257   $CePO_4$ could be either an experimental artifact [22, 23] or be caused by an isomorphic

258   second-order phase transition as the one occurring in monazite-type $PbCrO_4$ [13, 14].

259   Thus $CePO_4$ deserves to be systematically studied in future works.

260   A detailed discussion of the axial compressibilities of monazite $BiPO_4$ by means

261   of the compressibility tensor will be made in the next section. Here we will concentrate

262   on the RT EOS of the different phases obtained with the EosFit7c package [41]. For

263   phase II, the evolution of the volume with pressure can be well described by a 3rd order

264   Birch–Murnaghan (BM3) EOS [42] (see Fig. 6). The obtained EOS parameters are

265   given in Table II. Again theory and experiments compare quite well with each other.

266   From the determined bulk modulus at zero pressure, B_0, it can be concluded that

267   monazite-type $BiPO_4$ is more compressible than most rare-earth phosphates [17], but

268   has a B_0 comparable with that of $CePO_4$ [18]. A visual indication of the quality of the

269   EOS fit is provided in the inset of Fig. 6 where the normalized pressure (F) is plotted

270   versus the Eulerian strain (f_E) [43]. There it can be seen that the F–f_E relation lies on a

271   straight line with a positive slope, indicating that the experimental data are adequately

272   described by a BM3 EOS. From a linear least-squared fit to the F–f_E data we obtained

273     $B_0 = 101(1)$ GPa and $B_0' = 5.7(9)$ [43]. These values are consistent with those obtained

274   from the EOS fit to the experimental results.

275   For phase III we have also made an EOS fit to the P-V data. In this case, since

276   we have only five experimental data points we used a 2nd order Birch-Murnaghan

277   (BM2) EOS. The EOS parameters obtained are given in Table II. Again the agreement

278   between experiment and theory is quite good. Since B_0 and B_0' are correlated

279   parameters, to compare phase II with phase III we have also fit the results obtained for

280   phase II with a BM2 EOS. The obtained results are shown in Table II. There it can be

281   seen that phase III is much more compressible than phase II. In particular, the bulk

282   modulus at zero pressure, B_0, of $SbPO_4$-type $BiPO_4$ is comparable to that of $CrVO_4$-type

283   orthophosphates [35].

284   In Table II, we also give the theoretical EOS of phases I, IV, and V. Phase I is

285   the most compressible structure. A higher compressibility among orthophosphates is

286   only found in quartz-like and berlinite-type phosphates [44, 45]. Regarding phase IV,

287   we found that it is less compressible than the three ambient pressure polymorphs. The

288   increase of the bulk modulus in phase IV is related with the increase of the packing

289   efficiency in it. It is also important to note here that if a 4th order EOS is used to fit the

290   theoretical and experimental results, none of the four structures shows anomalous

positive values for the second pressure derivative of the bulk modulus (B_0''). This fact implies that the rate at which all phases become stiffer decreases with increasing pressure. On the other hand, from our calculations we conclude that in the five structures (found or predicted) in $BiPO_4$ the Bi-O bonds are much more compressible than the P-O bonds. Consequently they account for most of the volume reduction.

Regarding the scheelite phase, we would like to note that in spite of being the less compressible phase of $BiPO_4$, it still shows a bulk modulus (151 GPa) considerably smaller than the HP scheelite phases found in other trivalent metal phosphates [17] like scheelite-type $ScPO_4$ in which B0 = 376 GPa. Since the P-O bonds are known to be uncompressible [17, 39, 40], a possible explanation for this fact might be that Bi-O bonds are more compressible than Sc-O bonds. This hypothesis is consistent with the fact that all the know polimorphs of Bi_2O_3 has a bulk modulus ($B_0 < 100$ GPa) [46] which is considerable smaller than the bulk modulus of Sc_2O_3 ($B_0 = 188$ GPa) [47].

Let us now comment here on the potential hardness of scheelite-type $BiPO_4$. Several authors have demonstrated an empirical correlation between hardness and bulk modulus of materials [48]. By applying this correlation to scheelite-type $BiPO_4$, the Vickers hardness is estimated to be approximately 8 GPa, a value similar to that experimentally determined for related scheelite-type phosphates [49]. This is an interesting property which can be useful for technological applications since scheelite-type $BiPO_4$ can be potentially recovered as a metastable phase at ambient conditions. It would be also interesting to explore in the future the use of innovative preparation techniques of $BiPO_4$ nanoparticles [50] to explore the potential preparation of scheelite-type $BiPO_4$ nanostructures. Their preparation can be useful to enhance the photocatalytic activity of $BiPO_4$ since, for a given compound, scheelite phases are known to have a smaller electronic band gap than monazite phases [51].

316   Another fact to highlight is related to the EOS of phase V. According with our

317   calculations, the barite-type phase V has a bulk modulus smaller than scheelite-type

318   phase IV. This fact is apparently in contradiction with the density increase associated to

319   the scheelite-barite transition. However, similar phenomena, although not common,

320   have been also reported in other pressure-driven phase transitions; e.g. the B1–B2

321   transformation in alkali halides [52]. This phenomenon was assigned to a bond strength

322   decrease associated to the phase transition. This hypothesis is plausible in our case

323   where the coordination increase of Bi associated to the scheelite-barite transition is

324   accompanied by an increase of the average Bi-O interatomic distance.

325   **D. Isothermal compressibility tensor**

326   The isothermal compressibility tensor, β_{ij}, is a symmetric second rank tensor

327   which relates the state of strain of a crystal to the change in pressure that induced it [53].

328   This tensor for a monoclinic crystal has as coefficients:

329
$$\beta_{ij} = \begin{pmatrix} \beta_{11} & 0 & \beta_{13} \\ 0 & \beta_{22} & 0 \\ \beta_{13} & 0 & \beta_{33} \end{pmatrix}$$

330   Using the IRE (Institute of Radio Engineers) convention for the orthonormal

331   basis for the tensor: $e_3 \| c$, $e_2 \| b^*$, $e_1 \| e_2 \times e_3$, we have obtained the isothermal

332   compressibility tensor coefficients for phase II of $BiPO_4$ at a pressure of 2.4 GPa. The

333   tensor has been obtained using the linear Lagrangian approximation with the equations

334   given in Ref. [54] and with the infinitesimal Lagrangian approximation as implemented

335   in the Win-Strain package [55]. For the case of the linear Lagrangian approximation a

336   linear fit of the unit-cell parameters was carried out in the pressure range 0-4.8 GPa

337   where the unit-cell parameters behaviour was found to be linear. Table III reports the

338   values of the lattice parameters at 1 atm and their pressure derivatives from the linear

339   fits, which are used in the linear Lagrangian approximation, for the case of our

14

experimental and *ab initio* calculated data. Table III also includes the β_{ij} coefficients of the isothermal compressibility tensor with the two approximations used. It can be observed that the agreement between the experimental and calculated data is quite good. On the other hand, the β_{ij} coefficients obtained with the linear Lagrangian approximation agree, within the experimental uncertainties, with those obtained with the infinitesimal Lagrangian approximation as expected according to our small-strains assumption. The eigenvalues and eigenvectors for the isothermal compressibility tensor are reported in Table III. Taking into account the eigenvalues, it is found that for our experiments with the linear Lagrangian approximation, the maximum, intermediate and minimum compressibilities are $3.95(21) \times 10^{-3}$, $2.33(12) \times 10^{-3}$, and $1.84(21) \times 10^{-3}$ GPa^{-1}, respectively; whereas for the case of our calculations the obtained values for the compressibilities are 3.91×10^{-3}, 2.56×10^{-3} and 1.74×10^{-3} GPa^{-1}. These results indicate that around 50% of the total compression over the pressure range 0 - 4.8 GPa, is being accommodated along the direction of maximum compressibility. Taking into account the eigenvector ev_1, the major compression direction occurs in the (0 1 0) plane at the given angle Ψ (see Table III) to the c axis (from c to a). Note that the direction of maximum compressibility, taking into account the value of β_0, is at approximately 15º (21º) to the a axis for the case of our experimental (theoretical) data. The direction of intermediate compressibility (see eigenvector ev_2) is along the b axis, and the direction of minimum compressibility (see eigenvector ev_3) is in the (0 1 0) plane perpendicular to the direction of maximum compressibility. To conclude, we note that the isothermal compressibility tensor has not been obtained for phase III of BiPO$_4$ because of the small stability range of this monoclinic phase in which we have only structural information for the pure phase from our experiments at two different pressures, 0.1 and 0.6 GPa.

IV. Concluding remarks

In this work we reported an experimental and theoretical study of the structural stability of the different polymorphs of $BiPO_4$ under compression. XRD experiments together with calculations have allowed us to determine that phases I and III of $BiPO_4$ transform into the monazite-type polymorph (phase II) at very low pressure. Both phase transitions are irreversible. In addition, in our RT experiments it is found that phase II remains stable up to 31.5 GPa. In contrast, calculations predict a monazite $\rightarrow$ scheelite (phase IV) $\rightarrow$ barite (phase V) structural sequence under pressure. The monazite-scheelite transition was found experimentally upon the combined application of pressure and temperature, indicating that kinetic barriers may have hindered its finding at RT. The phase IV found experimentally has the scheelite crystal structure predicted by calculations. The barite phase V is theoretically predicted to occur at a pressure 20 GPa larger than the maximum pressure covered by our experiments. The RT equations of state of the different phases are also reported and discussed. Furthermore, the isothermal compressibility tensor is given for phase II at 2.4 GPa and its eigenvalues and eigenvectors are obtained providing information about the directions of maximum, intermediate and minimum compressibilities. Finally, the reported results are discussed in comparison with the HP structural behavior of related phosphates. We hope the results here reported will stimulate additional HP studies in $BiPO_4$ and related oxides.

Acknowledgements

390 **References**

391 [1] Q. Zhang, H. Tian, N. Li, M. Chen, and F. Teng, Cryst. Eng. Comm. **16**, 8334

392 (2014).

393 [2] C. Pan, D. Li, X. Ma, Y. Chen, and Y. Zhu, Catal. Sci. Technol. **1**, 1399 (2011)

394 [3] C. Pan, J. Xu, Y. Chen, and Y. Zhu, Appl. Catal. B **115**, 314 (2012).

395 [4] M. Zhao, G. Li, J. Zheng, L. Li, H. Wang, and L. Yang, Cryst. Eng. Comm. **13**,

396 6251 (2011).

397 [5] P. Arunkumar, C. Jayajothi, D. Jeyakumar, and N. Lakshminarasimhan, RSC Adv.

398 **2**, 1477 (2012).

399 [6] V. G. Alekseev, I. P. Gorelov, and M. V. Kornilov, J. Anal. Chem. **5**, 1055 (2005).

400 [7] I.-S. Cho, J. R. Kim, D. W. Kim, and K. S. Hong, J. Electroceram. **16**, 379 (2006).

401 [8] Z. Holgye and R. Poliak, J. Radioanal. Nucl. Chem. **153**, 267 (1991).

402 [9] Z. Holgye, J. Radioanal. Nucl. Chem. **12**, 227 (1998).

403 [10] S. N. Achary, D. Errandonea, A. Muñoz, P. Rodriguez-Hernadez, F. J. Manjon, P.

404 S. R. Krishna, S. J. Patwe, V. Grover, and A. K. Tyagi, Dalton Trans. **42**, 14999 (2013)

405 and references therein.

406 [11] Y. Ni, J. M. Hughes, and A. N. Mariano, Am. Mineral. **80**, 21(1995).

407 [12] R.M. Palin, M.P. Searle, M.R. St-Onge, D.J. Waters, N.M.W. Roberts, M.S.A.

408 Horstwood, R.R. Parish, O.M. Weller, S. Chen, amd J. Yang, Gondwana Research **26**,

409 323 (2014).

410 [13] D. Errandonea and R. S. Kumar, Mater. Res. Bull. **60**, 206 (2014).

411 [14] E. Bandiello, D. Errandonea, D. Martinez-Garcia, D. Santamaria-Perez, and F. J.

412 Manjón, Phys. Rev. B **85**, 024108 (2012).

413 [15] D. Errandonea, C. Popescu, S. N. Achary, A. K. Tyagi, and M. Bettinelli, Mater.

414 Res. Bull. **50**, 279 (2014).

415 [16] O. Ermakova, J. López-Solano, R. Minikayev, S. Carlson, A. Kamińska, M.

416 Głowacki, M. Berkowski, A. Mujica, A. Muñoz, and W. Paszkowicz, Acta Cryst. B **70**,

417 533 (2014).

418 [17] R. Lacomba-Perales, D. Errandonea, Y. Meng, and M. Bettinelli, Phys. Rev. B **81**,

419 064113 (2010).

420 [18] T. Huang, J. S. Lee, J. Kung, and C. M. Lin, Solid State Commun. **150**, 1845

421 (2010).

422 [19] A. Dewaele, P. Loubeyre, and M. Mezouar, Phys. Rev. B **70**, 094112 (2004).

423 [20] H. K. Mao, J. Xu, and P. M. Bell, J. Geophys. Res. **91**, 4673 (1986).

424 [21] S. Klotz, J. C. Chervin, P. Munsch, and G. L. Marchand, J. Phys. D: Appl. Phys.

425 **42**, 075413 (2009).

426 [22] D. Errandonea, A. Muñoz and J. Gonzalez-Platas, J. Appl. Phys. **115**, 216101

427 (2014).

428 [23] A. B. Garg, D. Errandonea, P. Rodríguez-Hernández, S. López-Moreno, A. Muñoz,

429 and C. Popescu, J. Phys.: Condens. Matter **26**, 265402 (2014).

430 [24] F. Fauth, I. Peral, C. Popescu, and M. Knapp, Powder Diffract. **28**, S360 (2013).

431 [25] D. Errandonea, D. Santamaria-Perez, T. Bondarenko, and O. Khyzhun, Mater. Res.

432 Bulletin **45**, 1732 (2010).

433 [26] A. P. Hammersley, S. O. Svensson, M. Hanfland, A. N. Fitch, and D. Häusermann,

434 High Pressure Res. **14**, 235 (1996).

435 [27] Oxford Diffraction (2006) CrysAllis Pro. Oxford Diffraction Ltd, Abingdon,

436 England.

437 [28] W. Kraus and G. Nolze, J. Appl. Crystallogr. **29**, 301 (1996).

438 [29] A. C. Larson and R. B. von Dreele, LANL Report 86–748 (2004).

439 [30] D. Errandonea, Phys. Rev. B **87**, 054108 (2013).

[31] D. Errandonea, J. Phys. Chem. Solids **67**, 2017 (2006).

[32] G. Kresse and D. Joubert, Phys. Rev. B **59**, 1758 (1999).

[33] J. P. Perdew, K. Burke and M. Ernzerhof, Phys. Rev. Lett. **77**, 3865 (1996).

[34] A. Mujica, A. Rubio, A. Muñoz and R. J. Needs, Rev. Mod. Phys. **75**, 863 (2003).

[35] S. López-Moreno and D. Errandonea, D., Phys. Rev. B **86**, 104112 (2012).

[36] D. Errandonea and F. J. Manjón, Prog. Mater. Sci. **53**, 711 (2008).

[37] O. Gomis, J. A. Sans, R. Lacomba-Perales, D. Errandonea, Y. Meng, J. C. Chervin, A. Polian, Phy. Rev. B **86**, 054121 (2012).

[38] D. Santamarıa-Perez, L. Gracia, G. Garbarino, A. Beltran, R. Chulia-Jordan, O. Gomis, D. Errandonea, Ch. Ferrer-Roca, D. Martinez-Garcıa, and A. Segura, Phys. Rev. B **84**, 054102 (2011).

[39] J. López-Solano, P. Rodríguez-Hernández, A. Muñoz, O. Gomis, D. Santamaría-Perez, D. Errandonea, F. J. Manjón, R. S. Kumar, E. Stavrou, and C. Raptis, Phys. Rev. B **81**, 144126 (2010).

[40] E. Stavrou, A. Tatsi, C. Raptis, I. Efthimiopoulos, K. Syassen, A. Muñoz, P. Rodríguez-Hernández, J. López-Solano, and M. Hanfland, Phys. Rev. B **85**, 024117 (2012).

[41] R. J. Angel, J. Gonzalez-Platas, and M. Alvaro, Z. Kristallogr. **229**, 405 (2014).

[42] F. Birch, J. Geophys. Res. 83 (1978) 1257.

[43] R. J. Angel, Rev. Mineral. Geochem. **41**, 35 (2000).

[44] J. Badro, J. P. Itie, and A. Polian, Eur. Phys. J. B **1**, 265 (1998).

[45] S. M. Sharma, N. Garg, and S. K. Sikka, J. Phys. Condens. Matter **12**, 6683 (2000).

[46] A.L.J. Pereira, D. Errandonea, A. Beltran, L. Gracia, O. Gomis, J.A. Sans, B. Garcıa-Domene, A. Miquel-Veyrat, F.J. Manjon, A. Muñoz, and C. Popescu, J. Phys.: Condens. Matter **25**, 475402 (2013).

465   [47] S. Barzilai, I. Halevy, and O. Yeheskel, J. Appl. Phys. **110**, 043532 (2011).

466   [48] R.J. Goble and S.D. Scott, Canadian Mineralogist **23**, 273 (1985).

467   [49] R. S. Hay, E. E. Boakye, and P. Mogilevsky, J. European Ceram. Society 34, 773

468   (2014).

469   [50] Q. Zhang, H. Tian, N. Li, M. Chen, and F. Teng, Crys. Eng. Comm. **16**, 8334

470   (2014).

471   [51] V. Panchal, D. Errandonea, A. Segura, P. Rodriguez-Hernandez, A. Muñoz, S.

472   Lopez-Moreno, and M. Bettinelli, J. Appl. Phys. **110**, 043723 (2011).

473   [52] A.M. Hofmeister, Phys. Rev. B **56**, 5835 (1997).

474   [53] S. Haussühl, Physical Properties of Crystals. An Introduction (Wiley-VCH, 2007).

475   [54] K. S. Knight, Phys. Chem. Minerals 37, 529 (2010).

476   [55] R. J. Angel. http://www.rossangel.com/text_strain.htm

477 **Table I:** Calculated atomic positions in scheelite-type $BiPO_4$ (top) at 27.6 GPa ($a =$

478 4.715 Å and $c = 11.064$ Å) and barite-type (bottom) $BiPO_4$ at 61.0 GPa ($a = 7.503$ Å, b

479 $= 4.715$ Å, and $c = 6.106$ Å). Wyckoff positions are indicated.

480

Atom	x	y	z
Bi (4b)	0	0.25	0.625
P (4a)	0	0.25	0.125
O (16f)	0.24030	0.12805	0.04842
Bi (4c)	0.17931	0.25	0.17797
P (4c)	0.06796	0.25	0.68685
O_1 (4c)	0.39975	0.25	0.94266
O_2 (4c)	0.23803	0.25	0.55725
O_3 (8d)	0.07841	0.50231	0.83470

481

482 **Table II:** EOS parameters for the different phases of $BiPO_4$. The last two columns

483 indicate the EOS type used and if results come from experiment (E) or theory (T).

Phase	V_0 [Å^3]	B_0 [GPa]	B_0'	EOS	
I	273.66	64.4	5.53	BM3	T
II	295.68	112.14	4.44	BM3	T
II	294.46	119.80	4	BM2	T
II	295.4(3)	99(2)	5.8(3)	BM3	E
II	294.2(2)	117(1)	4	BM2	E
III	160.42	88.18	2.92	BM3	T
III	160.01	84.8	4	BM2	T
III	160.0(2)	78(4)	4	BM2	E
IV	281.13	151.26	4.85	BM3	T
V	285.62	120.48	4.27	BM3	T

484

485   **Table III:** Lattice parameters at 1 atm, their pressure derivatives, the isothermal

486   compressibility tensor coefficients, β_{ij}, and their eigenvalues, λ_i, and eigenvectors, ev_i,

487   for monazite-BiPO$_4$ (phase II) at 2.4 GPa. The results are given using the linear

488   Lagrangian and the infinitesimal Lagrangian methods with data from our experiments

489   and our theoretical calculations.

Method	Linear Lagrangian		Infinitesimal Lagrangian	
	Experiment	Theory	Experiment	Theory
a_0 (Å), da/dP (Å·GPa^{-1})	6.756(1), -0.0256(7)	6.7554, -0.0246(5)		
b_0 (Å), db/dP (Å·GPa^{-1})	6.940(1), -0.0162(8)	6.9553, -0.0178(4)		
c_0 (Å), dc/dP (Å·GPa^{-1})	6.472(1), -0.0151(9)	6.47054, -0.0158(2)		
β_0 (°), dβ/dP (°·GPa^{-1})	103.65(5), -0.086(4)	103.954, -0.1033(8)		
β_{11} (10^{-3} GPa^{-1})	3.45(18)	3.21	3.50(13)	3.20
β_{22} (10^{-3} GPa^{-1})	2.33(12)	2.56	2.28(8)	2.57
β_{33} (10^{-3} GPa^{-1})	2.34(14)	2.44	2.16(8)	2.44
β_{13} (10^{-3} GPa^{-1})	-0.90(19)	-1.02	-0.96(13)	-1.03
λ_1 (10^{-3} GPa^{-1})	3.95(21)	3.91	4.01(14)	3.92
ev_1 (λ_1)	(0.873, 0, -0.487)	(0.822, 0, -0.570)	(0.886, 0, -0.463)	(0.821, 0, -0.571)
λ_2 (10^{-3} GPa^{-1})	2.33(12)	2.56	2.28(8)	2.57
ev_2 (λ_2)	(0, 1, 0)	(0, 1, 0)	(0, 1, 0)	(0, 1, 0)
λ_3 (10^{-3} GPa^{-1})	1.84(21)	1.74	1.66(14)	1.72
ev_3 (λ_3)	(0.487, 0, 0.873)	(0.570, 0, 0.822)	(0.463, 0, 0.886)	(0.571, 0, 0.821)
Ψ (°)[a]	119(4)	124.7	117.6(2.5)	124.8

490   [a] The major compression direction occurs in the (0 1 0) plane at the given angle Ψ to the c axis
491   (from c to a).

Figure captions

Figure 1: (color online) Schematic view of the crystal structure of different
polymorphs of $BiPO_4$. Bi atoms: purple, O atoms: red, P atoms: gray. The coordination
polyhedra are shown.

Figure 2: XRD patterns collected in run 1 up to 22 GPa. At selected pressures the
measured pattern (dots) is shown together with the calculated profile and residuals
(lines). The ticks indicate the position of Bragg reflections.

Figure 3: (color online) XRD patterns measured at 28 GPa before and after laser-
heating annealing and at 0.1 GPa after decompression. The measured patterns (dots) are
shown together with the calculated profiles and residuals (lines). The ticks indicate the
position of Bragg reflections.

Figure 4: (color online) (a) Energy vs volume and (b) enthalpy difference vs pressure
plots for the different structures of $BiPO_4$. To facilitate comparison, volumes have been
normalized assuming 4 formula units for all the structures. The structures have been
named as I, II, III, IV, and V following the main text.
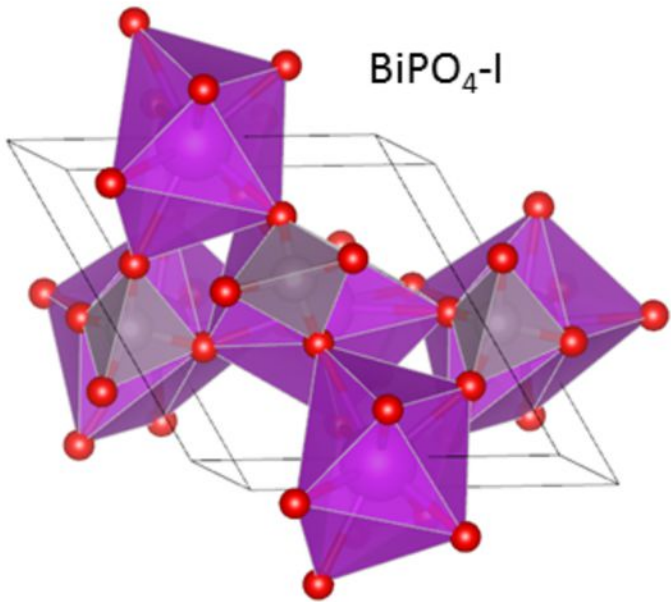
Figure 5: (color online) Pressure dependence of unit-cell parameters and volume for
phase III. Symbols: experiments. Solid lines: fitted BM2 EOS for volume and guides to
the eye for *a*, *b*, *c*, and *β*. Dashed lines: calculations.
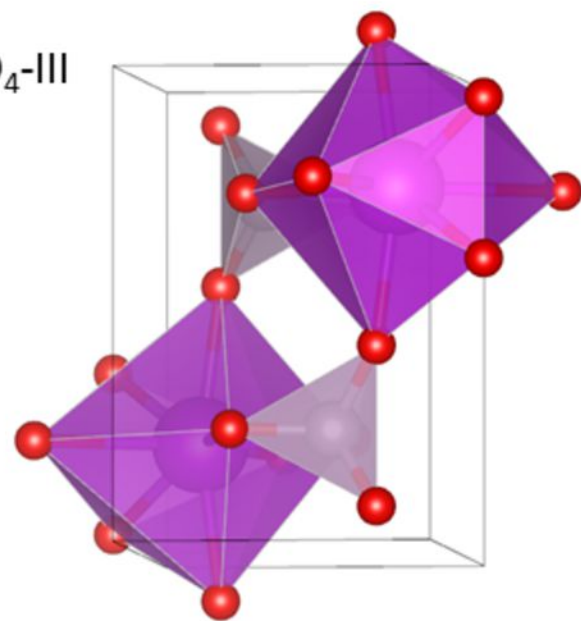
Figure 6: (color online) Pressure dependence of unit-cell parameters and volume for
phase II. Symbols: experiments, ● run 1, ▲ run 2, ■ run 3, and ▼ run 4. Solid lines:
fitted BM3 EOS for volume and guides to the eye for *a*, *b*, *c*, and β. Dashed lines:
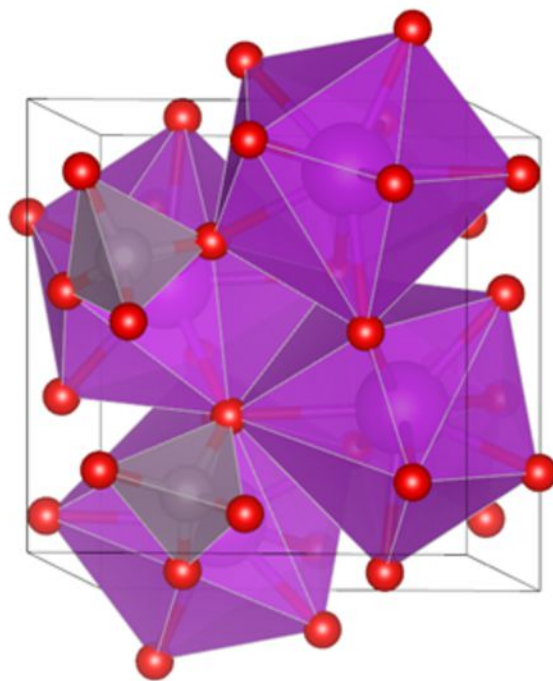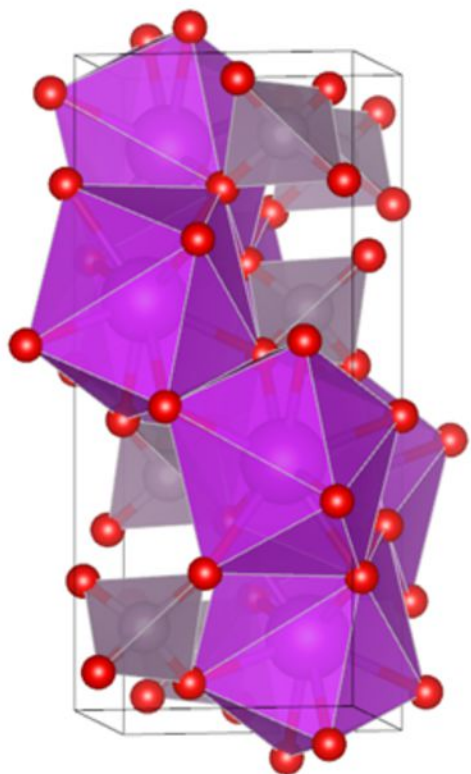calculations. The inset shows the normalized pressure vs Eulerian strain (F–f_E) plot.

BiPO$_4$-I BiPO$_4$-III BiPO$_4$-II BiPO$_4$-IV BiPO$_4$-V

Phase II
22 GPa
W

Phase II
9.9 GPa
W

Phase II
4.2 GPa
W

Coexistence
3.0 GPa
W
* * * * * *

Coexistence
0.8 GPa
W
* * * *

Phase III
0.6 GPa
W

Phase III
0.1 GPa
W

Intensity (arb. units)

6   9   12   15

2θ (degrees)

(a)

(b)